

Deep Models, Shallow Alignment: Uncovering the Granularity Mismatch in Neural Decoding

Yang Du¹ Siyuan Dai¹ Yonghao Song² Paul M. Thompson³
 Haoteng Tang⁴ Liang Zhan¹

¹Dept. of Electrical & Computer Engineering, University of Pittsburgh, USA

²Dept. of Biomedical Engineering, Tsinghua University, China

³Dept. of Neurology, University of Southern California, USA

⁴Dept. of Computer Science, University of Texas Rio Grande Valley, USA

liang.zhan@pitt.edu

Abstract

Neural visual decoding is a central problem in brain–computer interface research, aiming to reconstruct human visual perception and to elucidate the structure of neural representations. However, existing approaches overlook a fundamental granularity mismatch between human and machine vision, where deep vision models emphasize semantic invariance by suppressing local texture information, whereas neural signals preserve an intricate mixture of low-level visual attributes and high-level semantic content. To address this mismatch, we propose Shallow Alignment, a novel contrastive learning strategy that aligns neural signals with intermediate representations of visual encoders rather than their final outputs, thereby striking a better balance between low-level texture details and high-level semantic features. Extensive experiments across multiple benchmarks demonstrate that Shallow Alignment significantly outperforms standard final-layer alignment, with performance gains ranging from 22% to 58% across diverse vision backbones. Notably, our approach effectively unlocks the scaling law in neural visual decoding, enabling decoding performance to scale predictably with the capacity of pre-trained vision backbones. We further conduct systematic empirical analyses to shed light on the mechanisms underlying the observed performance gains.

1 Introduction

Understanding how the brain encodes visual information is a fundamental problem in both neuroscience and artificial intelligence[18, 37, 28, 40, 25]. Recent advances in brain-computer interfaces, particularly studies based on electroencephalography (EEG) and magnetoencephalography (MEG), have demonstrated the feasibility of decoding visual stimuli directly from neural activity [34, 15, 17, 33]. This task, commonly referred to as neural visual decoding, aims to retrieve perceived visual stimuli from non-invasive neural recordings. The core challenge lies in learning an alignment function that can translate high-dimensional, noisy neural dynamics into structured visual representations.

The prevailing paradigm in neural visual decoding adopts large-scale pre-trained vision models (e.g., CLIP) as feature extractors, aligning neural signals to visual representations via contrastive learning on the final-layer embeddings of these models [32, 23, 43, 39, 44]. However, these approaches overlook a fundamental granularity mismatch between human and machine vision. The inductive bias of contemporary vision models aims to maximize semantic invariance, systematically discarding local variations to optimize for categorization [21, 30, 20]. In contrast, visually evoked neural responses are not confined to a single level of abstraction. Instead, they encode information across multiple representational scales, ranging from low-level attributes such as contours, color, and spatial frequency to high-level semantic content. [7, 3, 6, 11]. As a result, aligning neural signals to the final, most abstract layer of vision models forces a complex, multi-scale neural representation to match a

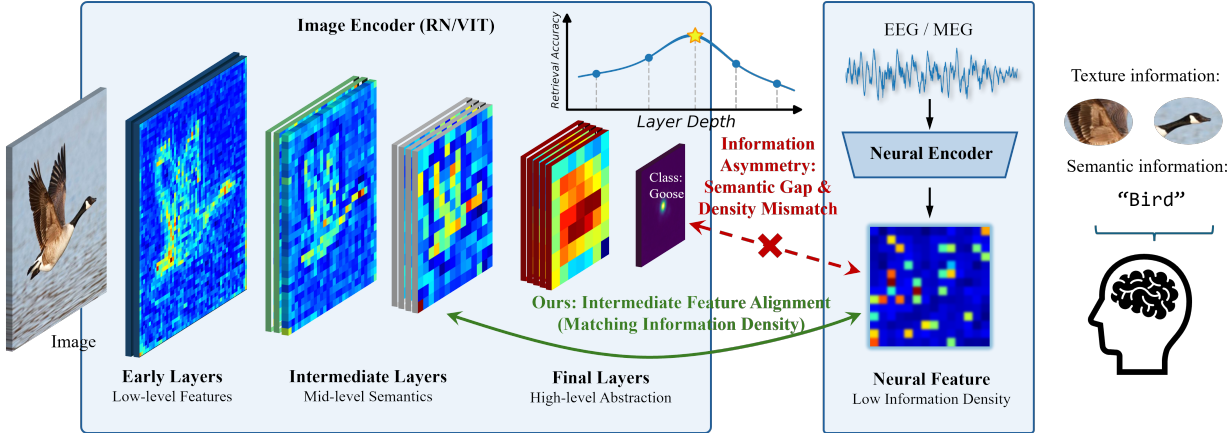


Figure 1: Overview of the proposed Shallow Alignment framework. The model aligns neural signals with intermediate visual representations to mitigate information-lossy alignment at high semantic levels.

texture-insensitive semantic embedding. This granularity mismatch introduces significant ambiguity into the contrastive objective, as distinct neural patterns with differing low-level characteristics may be mapped to similar high-level visual representations. Consequently, the resulting supervision signal is insufficiently informative to guide effective neural representation learning.

To bridge this gap, we propose Shallow Alignment, a strategy that shifts the neural decoding target from the final output layer to the intermediate layers of vision encoders. We posit that intermediate representations offer a more appropriate granularity match for non-invasive neural signals, balancing high-level semantic abstraction with the retention of structural fidelity.

Our contributions are summarized as follows:

- We propose Shallow Alignment, a neural visual decoding framework that mitigates the granularity mismatch between neural signals and vision encoders, yielding consistent improvements across multiple benchmarks.
- We resolve a Depth–Capacity Paradox, where increased semantic abstraction in deeper layers hinders effective alignment. By addressing this, we unlock the scaling law for neural decoding, enabling performance to scale with model capacity.
- Through extensive empirical analysis showing superior alignment with intermediate layers, we provide evidence for a shared hierarchical granularity between human visual processing and deep vision models.

2 Related Work

2.1 Semantic Granularity in Neural Decoding

Recent advancements in neural decoding have predominantly focused on aligning neural signals with the latent spaces of large-scale pre-trained vision models. [32] introduced a contrastive learning approach that incorporates plug-and-play self-attention and graph attention modules to capture spatial correlations in EEG electrodes for effective image decoding. [23] proposed an end-to-end zero-shot framework that utilizes a tailored EEG encoder named Adaptive Thinking Mapper (ATM)

to align EEG signals with CLIP embeddings. Leveraging contrastive learning, [43] developed a method to align EEG signals not only with images but also with generated captions and depth maps, demonstrating that complementary multimodal information enhances brain signal decoding. However, emerging evidence suggests that maximizing semantic abstraction does not necessarily yield optimal decoding performance. For instance, [39] identified a "System GAP" between human perception and digital stimuli, proposing an Uncertainty-Aware Blur Prior (UBP) that improves alignment by dynamically adjusting the blur radius based on sample uncertainty. Similarly, [44] introduced NeuroBridge leverages Cognitive Prior Augmentation to simulate perceptual variability via image transformations, including Gaussian blur, Gaussian noise, mosaic effects, and low-resolution downsampling. Notably, they also reported a counter-intuitive phenomenon where architecturally simpler backbones (e.g., ResNet-50) often exhibit competitive or even superior performance compared to large-scale foundation models (e.g., ViT) under standard settings. This observation motivates our hypothesis that the key to alignment lies not in maximizing semantic level of the image or neural representation, but in precisely calibrating the representational granularity between modalities.

2.2 Hierarchical Representations in Human and Artificial Vision

Neuroscience has established that the primate visual cortex operates via a cascade of processing stages, where early areas (e.g., V1, V2) encode low-level features like spatial frequencies and orientation, while high-level object semantics emerge only in later stages (e.g., IT cortex)[7, 6]. An interesting parallelism exists in deep artificial neural networks, which evolve from detecting low-level primitives in shallow layers to representing abstract concepts in deep layers[41, 26]. In addition, non-invasive neural recordings (e.g., EEG/MEG) are inherently noisy and characterized by sparse information density. They are susceptible to multiple sources of contamination, including environmental interference, muscle artifacts, and intrinsic biological variability, leading to substantially reduced signal-to-noise ratios[13, 35]. We posit that these create a fundamental granularity mismatch, where the intricate feature granularity of the brain signals is incompatible with the highly abstract, semantically compressed representations at the final output of the model.

2.3 Granularity Balance in Intermediate Representations

Prior research has demonstrated the utility of intermediate layers for diverse tasks, ranging from elucidating training dynamics [1] to enhancing transfer learning [9] and improving robustness against distribution shifts [22, 36]. Crucially, these works point to a fundamental trade-off in feature evolution. As networks deepen, they undergo Neural Collapse [30], where class representations inevitably collapse toward their mean centers in the final layer to maximize separability. Although advantageous for classification, this abstraction process severely compresses the feature manifold and reduces its intrinsic dimensionality [2], filtering out the structural details critical for fidelity reconstruction. In contrast, intermediate layers maintain a Granularity Balance: they possess sufficient semantic density to distinguish concepts while retaining the high intrinsic dimensionality and structural redundancy. We argue that this characteristic makes intermediate layers, rather than the collapsed final output, superior alignment target for neural visual decoding.

3 Methodology

As illustrated in Figure 1, we propose Shallow Alignment, which mitigates the granularity mismatch between neural signals and visual representations.

3.1 Problem Definition

We formulate neural visual decoding as a cross-modal representation alignment problem between neural signals and visual stimuli. Let $\mathcal{D} = (x_N^{(k)}, x_I^{(k)})_{k=1}^M$ denote a paired dataset of M samples, where $x_N^{(k)} \in \mathbb{R}^{C \times T}$ represents a non-invasive neural signal with C channels and T time points, and $x_I^{(k)} \in \mathbb{R}^{H \times W \times 3}$ denotes the corresponding visual stimulus. The objective is to learn a neural encoder $f_\theta : \mathcal{X}_N \rightarrow \mathcal{Z}$ that maps raw neural signals into a latent embedding space \mathcal{Z} , aligning them with visual representations extracted by a pre-trained vision encoder E_ϕ . In conventional approaches, the neural embedding $z_N = f_\theta(x_N)$ is aligned with the final-layer output of the vision encoder, denoted as $z_{\text{last}} = E_\phi(x_I)$. However, the final-layer representation z_{last} is typically a highly compressed and semantically abstract embedding in which local structural information is largely suppressed. Aligning such representations with noisy and multi-scale neural signals exacerbates a granularity mismatch between these two modalities.

3.2 Pretrained Vision Models

For the vision encoder E_ϕ , we consider a diverse set of pre-trained visual backbones, ranging from conventional convolutional architectures to large-scale Vision Transformers. Specifically, we include ResNet-50 and ResNet-101 [16], as well as Vision Transformer models of increasing capacity, including ViT-B/16 [8], ViT-H/14 [42], and ViT-bigG/14 [5], all using pretrained weights provided by OpenCLIP[19]. To systematically study the effect of model scale and architecture on neural visual decoding, we further incorporate several state-of-the-art large-scale visual encoders, including DINOv2 [29], EVA-02 [10], and InternViT [4].

3.3 Shallow Alignment via Intermediate Representations

To mitigate the granularity mismatch, we introduce Shallow Alignment, which shifts the alignment target from the final output to intermediate representations of the vision encoder. Consider a deep vision encoder E_ϕ composed of L layers. Given an input image x_I , the encoder produces a sequence of hidden representations $\mathbf{H} = \{h^{(1)}, h^{(2)}, \dots, h^{(L)}\}$, where $h^{(l)}$ denotes the feature map at the l -th layer.

In contrast to the final embedding z_{last} , which is optimized for semantic invariance and is largely insensitive to local spatial variations, intermediate representations capture a more balanced level of abstraction. In particular, the representation at a selected depth l^* preserves informative structural details while remaining sufficiently discriminative at the semantic level.

Formally, we define the target visual embedding z_I as the pooled feature from the intermediate layer l^* :

$$z_I = \text{Pool}\left(h^{(l^*)}(x_I)\right), \quad 1 \leq l^* < L \quad (1)$$

where $\text{Pool}(\cdot)$ denotes a pooling operation that aggregates spatial features into a fixed-dimensional vector.

3.4 Linear Semantic Projector

To align the two modalities, we project the neural features z_N and visual features z_I into a shared latent space using linear mappings:

$$\mathbf{v} = W_N z_N + b_N, \quad \mathbf{w} = W_I z_I + b_I, \quad (2)$$

where W_N and W_I are learnable projection matrices, and b_N and b_I denote bias terms.

These linear transformations act as learnable projections that distill high-dimensional, redundant intermediate features into a latent subspace aligned with the neural manifold. By restricting the projection to be linear, we explicitly limit model capacity, encouraging the alignment performance to stem from the quality of the intermediate representations themselves rather than from expressive but potentially overfitting decoders.

3.5 Contrastive Objective

We employ a symmetric contrastive objective [31] that encourages matched neural–visual pairs $(\mathbf{v}^{(k)}, \mathbf{w}^{(k)})$ to exhibit high similarity, while separating mismatched pairs within each mini-batch. The contrastive loss is defined as

$$\begin{aligned} \mathcal{L}_C = & -\frac{1}{2M} \sum_{k=1}^M \left[\log \frac{\exp(\text{sim}(\mathbf{w}^{(k)}, \mathbf{v}^{(k)})/\tau)}{\sum_{j=1}^M \exp(\text{sim}(\mathbf{w}^{(k)}, \mathbf{v}^{(j)})/\tau)} \right. \\ & \left. + \log \frac{\exp(\text{sim}(\mathbf{v}^{(k)}, \mathbf{w}^{(k)})/\tau)}{\sum_{j=1}^M \exp(\text{sim}(\mathbf{v}^{(k)}, \mathbf{w}^{(j)})/\tau)} \right], \end{aligned} \quad (3)$$

where $\text{sim}(\cdot, \cdot)$ denotes cosine similarity, τ is a temperature hyperparameter, and M denotes the number of paired samples in the batch. This bidirectional formulation enforces consistent alignment across modalities and is used as the primary training objective[38].

4 Experiments

4.1 Datasets

THINGS-EEG [12, 15] provides high-density electroencephalography (EEG) recordings from 10 participants collected under a Rapid Serial Visual Presentation (RSVP) paradigm[14]. It comprises a training set of 1,654 unique object concepts and a disjoint test set of 200 concepts. For training, each concept is associated with 10 distinct images, each presented 4 times. In the test set, a single image is used per concept and repeated 80 times.

THINGS-MEG [17] contains magnetoencephalography (MEG) recordings from 4 participants and covers a total of 2,054 object concepts. The dataset is partitioned into 1,854 training concepts and 200 testing concepts. During training, each concept includes 12 distinct images, whereas the test set consists of 12 repeated presentations of a single image per concept.

For data preprocessing, we follow the methodology described in previous work[39, 44]. Comprehensive details are provided in Appendix A.1.

4.2 Implementation Details

All experiments are implemented in PyTorch and conducted on NVIDIA GeForce RTX 3090 GPUs. We utilize EEGProject as the neural encoder and select the channels corresponding to the overlying occipital and parietal cortex related to visual. Models are trained for 50 epochs with a batch size of 1,024 using the AdamW optimizer, with a learning rate of 1×10^{-4} and a weight decay of 1×10^{-4} . For evaluation, we compute retrieval accuracy using cosine similarity between neural and image embeddings, reporting Top-1 and Top-5 accuracies under intra-subject and inter-subject settings. Reported results are averaged over five independent runs with different random seeds.

Table 1: Overall accuracy (%) of 200-way zero-shot retrieval on THINGS-EEG: Top-1 and Top-5.

Method	Metric	Sub1	Sub2	Sub3	Sub4	Sub5	Sub6	Sub7	Sub8	Sub9	Sub10	Avg.
Intra-Subject: train and test on one subject												
NICE	Top-1	13.2	13.5	14.5	20.6	10.1	16.5	17.0	22.9	15.4	17.4	16.1
	Top-5	39.5	40.3	42.7	52.7	31.5	44.0	42.1	56.1	41.6	45.8	43.6
ATM	Top-1	25.6	22.0	25.0	31.4	12.9	21.3	30.5	38.8	34.4	29.1	27.1
	Top-5	60.4	54.5	62.4	60.9	43.0	51.1	61.5	72.0	51.5	63.5	58.1
Neural-MCRL	Top-1	27.5	28.5	37.0	35.0	22.5	31.5	31.5	42.0	30.5	37.5	32.4
	Top-5	64.0	61.5	69.0	66.0	51.5	61.0	62.5	74.5	59.5	71.0	64.1
UBP	Top-1	41.2	51.2	51.2	51.1	42.2	57.5	49.0	58.6	45.1	61.5	50.9
	Top-5	70.5	80.9	82.0	76.9	72.8	83.5	79.9	85.8	76.2	88.2	79.7
NeuroBridge	Top-1	50.0	63.2	61.6	61.4	54.8	69.7	62.7	71.2	64.0	73.6	63.2
	Top-5	77.6	90.6	91.1	90.0	85.0	92.9	88.8	95.1	91.0	97.1	89.9
Ours	Top-1	75.0	87.5	83.2	79.5	74.6	89.9	78.5	86.9	81.3	89.3	82.6
	Top-5	94.3	98.9	98.2	96.1	96.4	99.3	97.3	99.4	97.8	99.1	97.7
Inter-Subject: leave one subject out for test												
NICE	Top-1	7.6	5.9	6.0	6.3	4.4	5.6	5.6	6.3	5.7	8.4	6.2
	Top-5	22.8	20.5	22.3	20.7	18.3	22.2	19.7	22.0	17.6	28.3	21.4
ATM	Top-1	10.5	7.1	11.9	14.7	7.0	11.1	16.1	15.0	4.9	20.5	11.9
	Top-5	26.8	24.8	33.8	39.4	23.9	35.8	43.5	40.3	22.7	46.5	33.8
Neural-MCRL	Top-1	13.0	12.0	14.5	12.5	11.5	13.5	14.0	18.5	13.5	17.0	14.0
	Top-5	31.5	30.5	35.5	35.5	29.0	35.5	36.0	38.5	32.5	39.0	34.3
UBP	Top-1	11.5	15.5	9.8	13.0	8.8	11.7	10.2	12.2	15.5	16.0	12.4
	Top-5	29.7	40.0	27.0	32.3	33.8	31.0	23.8	32.2	40.5	43.5	33.4
NeuroBridge	Top-1	23.2	21.2	13.2	17.0	14.5	25.0	15.3	20.1	13.7	27.2	19.0
	Top-5	52.4	49.3	36.5	45.3	37.7	55.0	45.1	44.9	36.5	56.3	45.9
Ours	Top-1	23.5	30.6	10.0	19.5	18.1	22.7	18.6	17.3	23.0	34.4	21.8
	Top-5	53.2	60.4	28.1	48.3	45.2	49.8	46.0	46.1	54.8	62.0	49.4

4.3 Bridging Cross-Modal Granularity Mismatch via Intermediate-Layer Alignment

We compared our Shallow Alignment strategy against state-of-the-art methods, including NICE[32], ATM[23], Neural-MCRL[24], NeuroBridge[44], on both THINGS-EEG and THINGS-MEG datasets.

As shown in Table 1, our method achieves substantial improvements across all evaluation metrics. Baseline approaches such as NICE, ATM, and Neural-MCRL primarily aim to enhance alignment with high-level semantic representations, while largely neglecting the granularity mismatch between neural signals and visual features, potentially limiting retrieval performance.

UBP and NeuroBridge improve performance to 50.9% and 63.2% Top-1 accuracy, respectively, by incorporating data augmentation strategies. Although these gains are commonly attributed to improved robustness against perceptual variability and low-level acquisition noise, the observed improvements can also be interpreted as arising from implicit granularity adaptation. By blurring or perturbing images, these methods attenuates fine-grained texture details. This reduction in visual complexity shifts the feature manifold to a lower granularity, thereby enabling a more robust match with the coarse and noisy neural recordings. However, this improved alignment comes at the expense of high-fidelity information for accurate neural decoding.

In contrast, our method explicitly aligns neural signals with intermediate visual representations,

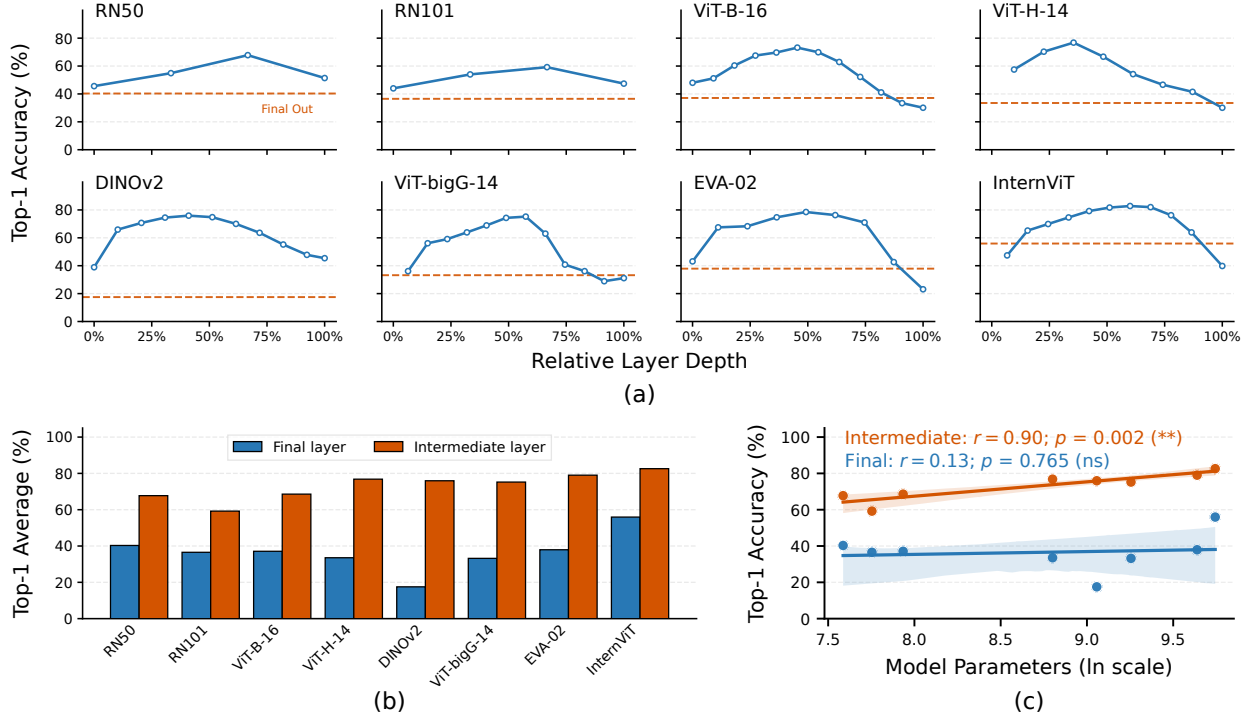


Figure 2: Comparative analysis of representational performance between intermediate and final layers on THINGS-EEG. (a) Top 1 accuracies of intermediate features across vision backbones. Relative depth is computed as $(\ell - 1)/(L - 1)$. Dashed orange lines mark the Final Output performance. For ResNet models, the final feature is obtained by attention pooling of the last convolutional layer. For Transformer-based models, the final feature corresponds to the CLS token embedding from the last layer. (b) Performance comparison across architectures. The bar chart summarizes the Top-1 accuracy gap between the best-performing intermediate layer (orange) and the final output layer (blue). (c) Scaling analysis. Linear regression analysis reveals the relationship between model scale (number of parameters in ln scale) and Top-1 accuracy. Statistical significance is denoted by asterisks (** for $p < 0.01$) or by “ns” for non-significant results ($p > 0.05$).

directly exploiting shared structural properties between the human visual system and deep vision models. This design leads to a more appropriate granularity match and results in a Top-1 accuracy of 82.6% under the intra-subject retrieval setting. These results indicate that addressing granularity mismatch plays a critical role in improving neural visual decoding performance. Under the inter-subject setting, our method also yields consistent gains. However, the improvement (2.8% Top-1 accuracy) remains limited, suggesting the presence of an additional between-subject granularity mismatch that is not fully addressed.

A consistent trend is observed on the THINGS-MEG dataset (Table 2). Under the intra-subject protocol, our method achieves 48.0% Top-1 accuracy and 74.4% Top-5 accuracy, substantially outperforming NeuroBridge (32.2% / 60.8%) and UBP (26.7% / 55.2%). Nevertheless, performance remains low for all methods in the inter-subject setting, which may reflect a more pronounced between-subject granularity mismatch in MEG recordings.

Table 2: Overall accuracy (%) of 200-way zero-shot retrieval on THINGS-MEG: Top-1 and Top-5.

Method	Metric	Sub1	Sub2	Sub3	Sub4	Avg.
Intra-subject: train and test on the same subject						
UBP	Top-1	15.0	46.0	27.3	18.5	26.7
	Top-5	38.0	80.5	59.0	43.5	55.2
NeuroBridge	Top-1	16.5	53.7	40.4	18.1	32.2
	Top-5	41.6	85.3	73.2	43.1	60.8
Ours	Top-1	25.5	81.9	56.0	28.6	48.0
	Top-5	54.5	97.4	87.5	58.3	74.4
Inter-subject: leave-one-subject-out (LOSO)						
UBP	Top-1	2.0	1.5	2.7	2.5	2.2
	Top-5	5.7	17.2	10.5	8.0	10.4
NeuroBridge	Top-1	4.3	3.6	3.0	2.5	3.4
	Top-5	13.1	15.6	11.2	11.3	12.8
Ours	Top-1	1.3	6.6	5.4	1.5	3.7
	Top-5	6.9	18.5	18.5	7.9	13.0

4.4 Unlocking Scaling Laws via Granularity-Matched Alignment

We extend our evaluation across a diverse set of vision backbones that vary in architecture, training objectives, and model scale. For relatively shallow architectures (e.g., ResNet), we evaluate representations from all layers. For ultra-deep Transformer-based models, we adopt a uniform sampling strategy, probing approximately ten evenly spaced intermediate layers to estimate layer-wise performance. The results are summarized in Figure 2.

Across models, the Top-1 retrieval accuracy exhibits a consistent inverted U-shaped trend as a function of layer depth, first increasing and then declining. This behavior aligns with the hierarchical nature of visual representations in deep networks, where early layers capture low-level texture information and deeper layers progressively encode more abstract semantic concepts. As a result, representations at different depths correspond to different degrees of semantic–texture entanglement. We argue that peak performance occurs when the granularity of the visual feature mixture most closely matches the inherent characteristics of neural signals, creating an optimal bridge for alignment. As illustrated in Figure 2(a), different models possess unique feature extraction capabilities, leading to distinct dynamic balances between texture and semantic information across their layers. For instance, ViT-H/14 achieves peak performance at approximately 35.5% of its relative depth, whereas InternViT peaks at around 60%. Detailed results are provided in Appendix B.1.

As shown in Figure 2(b), conventional alignment using only the final output layer reveals a counterintuitive trend: increasing model size does not necessarily improve neural decoding performance. In fact, large-scale models often underperform due to excessive semantic abstraction at their final layers. For example, DINOv2 achieves a Top-1 accuracy of only 17.5% when aligned at its final layer, substantially lower than the performance of the much smaller ResNet-50 (40.3%). This observation indicates that highly compressed and invariant final-layer representations are poorly matched to neural signals, as they discard fine-grained structural information. In contrast, selecting an appropriate intermediate layer fundamentally alters this behavior. When alignment is performed at the optimal depth, a clear scaling trend emerges: decoding performance consistently improves with increasing model capacity (see Figure 2(c)). The most significant gain is observed in DINOv2, which improves by 58.4% when shifting the alignment target from the final output to its optimal intermediate representation.

Taken together, these results indicate that the primary bottleneck in neural visual decoding is not the quality of visual representations in large models, but the choice of alignment target. By calibrating representational granularity through intermediate-layer alignment, Shallow Alignment enables effective utilization of the representational capacity of large-scale vision models.

4.5 Revealing Performance Trade-offs via Concept Analysis

We report *Concept Accuracy*, defined as the proportion of Top-5 retrieved images that share the same concept category (animals, food, vehicles, tools, clothing, or others) as the query, excluding the query image itself. Formally, for each query, we count the number of concept-matched items within the Top-5 results and normalize by $5M$, where M denotes the number of queries.

As illustrated in Figure 3, layer-wise analysis reveals a clear divergence between concept accuracy and retrieval accuracy. Concept accuracy increases monotonically with network depth, reflecting progressively stronger semantic abstraction. In contrast, Top-1 retrieval accuracy follows a non-monotonic trend, peaking at an intermediate layer and declining sharply at the final layer. This behavior aligns with observations from the human visual system, which integrates mid-level visual cues (e.g., contours and texture) together with high-level semantic information, rather than collapsing representations purely to category identity. As a result, improvements in semantic consistency alone do not guarantee better retrieval performance. Instead, retrieval accuracy is maximized when visual representations preserve fine-grained structural details while maintaining sufficient semantic coherence.

These results indicate that the performance degradation observed at the final layer is not caused by insufficient semantic representation, but by the loss of texture-level information in highly abstract visual features. By retaining such details, intermediate representations achieve a more favorable balance between semantic correctness and discriminative precision. Figure 4 presents representative examples of the Top-5 retrieval results.

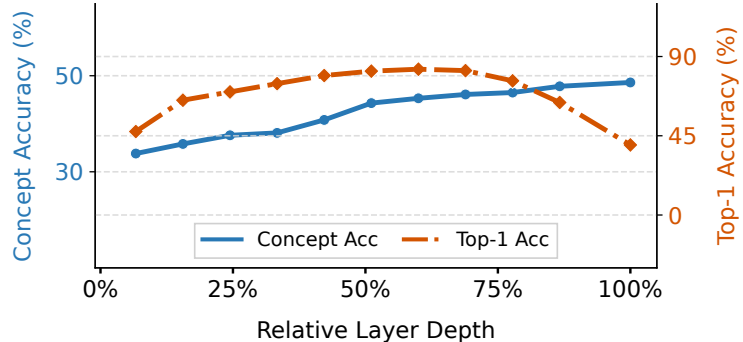


Figure 3: Concept accuracy and retrieval Top-1 accuracy on THINGS-EEG versus layer depth for InternViT. Relative depth is computed as $(\ell - 1)/(L - 1)$.



Figure 4: Top-5 retrieved samples of Subject 7 on THINGS-EEG. (a) Retrieval based on the best intermediate-layer embeddings. (b) Retrieval based on final output embeddings. The red box indicates the ground-truth target.

4.6 Visualizing Granularity Consistency via Manifold Distributions

We employ UMAP [27] to visualize the geometric distributions of the projected neural embeddings \mathbf{v} and visual embeddings \mathbf{w} on the test set. As shown in Figure 5, when alignment is performed at the early layer or the final output layer, the embeddings from the two modalities form clearly separated clusters with distinct boundaries. This separation reflects a pronounced modality gap, indicating that the granularity of these layer visual representations is poorly matched to that of neural signals. In contrast, at the proper intermediate layer, EEG and visual embeddings substantially overlap and intermingle in the projected space. This observation suggests that intermediate representations induce a manifold structure whose granularity is more consistent with neural signals, thereby supporting more effective alignment. More visualization results are provided in Appendix B.3.

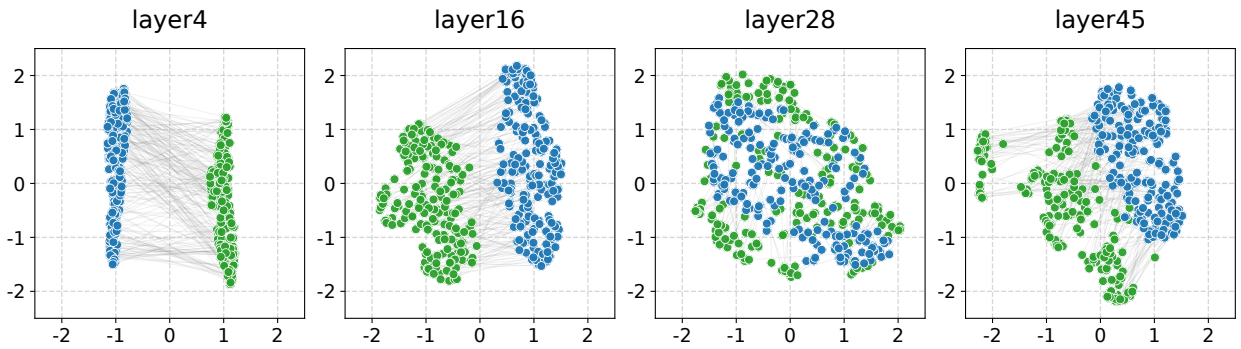


Figure 5: UMAP visualization of cross-modal alignment on THINGS-EEG (Subject 7). We illustrate the feature alignment between EEG signals and visual representations on the test set ($M = 200$). Image features are extracted from selected intermediate layers versus the final output layer, aligned with EEG embeddings from the neural encoder. Gray lines connect ground-truth image-EEG pairs.

4.7 Validating Semantic Collapse via Linear Projection Ablation

We conduct an ablation study on the linear projection to examine its role in alignment. As shown in Figure 6, we observe a clear contrast in the effectiveness of linear projection across different representation depths. When applied to the final-layer visual embeddings, introducing a learnable

linear projector yields only marginal performance improvements. In contrast, linear projection substantially improves alignment performance when applied to intermediate representations. The most pronounced gain is observed for ResNet-50, where Top-1 accuracy increases from 28.8% to 67.7%, corresponding to an absolute improvement of nearly 40%. The limited benefit at the final layer suggests that these representations have undergone severe semantic collapse, such that a simple linear transformation is insufficient to recover the structural information necessary for effective alignment. Conversely, the significant improvements observed at intermediate layers indicate that these representations retain richer structural fidelity. This richness allows the linear layer to function as a selective filter, identifying the specific visual primitives that best match the granularity of neural signals while discarding task-irrelevant noise.

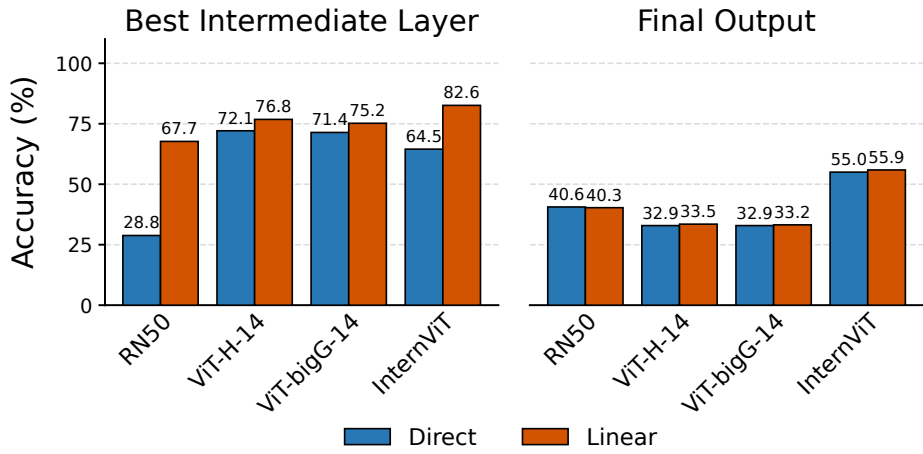


Figure 6: Top 1 accuracy comparison across different projector types on THINGS-EEG. Results are shown for the best intermediate layer and the final output layer.

4.8 Evaluating Encoder Efficacy via Architectural Comparison

To assess the impact of encoder architecture on cross-modal alignment performance, we examine combinations of five EEG encoders and eight vision encoders (See details in Appendix A.2). Our empirical evaluation highlights the superior efficacy of EEGProject. Despite its architectural simplicity, it outperforms more complex baselines (e.g., EEGNet, ATM).

As shown in Figure 7, the lightweight EEGProject model consistently attains the highest performance across all vision backbones, achieving the highest average accuracy of 73.1%. This outcome aligns with the intrinsic nature of EEG data, which is characterized by a low signal-to-noise ratio and data scarcity. In this regime, complex architectures struggle to generalize. For instance, despite its high capacity, the widely used EEGNet averages only 53.8% accuracy, lagging behind our simpler MLP-based approach by nearly 20%.

Conversely, EEGProject imposes a tighter information bottleneck that forces the encoder to distill the most discriminative features while suppressing task-irrelevant artifacts. This results in representations that are better aligned with the visual embedding space. These findings suggest that, for neural visual decoding, a simple architecture can be more effective when paired with appropriately chosen visual representations.

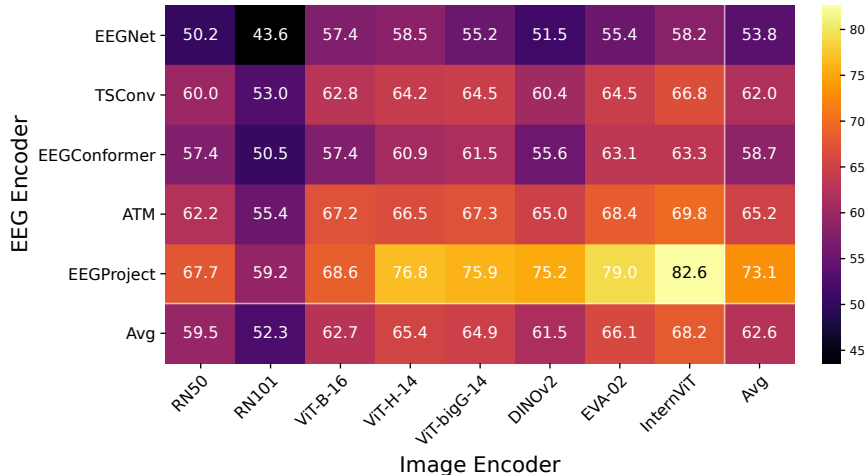


Figure 7: Top-1 accuracy (%) for various encoders architectures on THINGS-EEG.

5 Conclusion

In this work, we expose a fundamental granularity mismatch in neural visual decoding. Non-invasive neural signals retain multi-scale visual information, while deep vision models progressively collapse representations into highly abstract, semantically compressed embeddings. By shifting the alignment target to intermediate representations, our Shallow Alignment not only resolves this mismatch but also, crucially, unlocks the scaling laws of large vision models for neural decoding. Beyond substantial performance gains, the effective alignment of neural signals with intermediate representations serves as empirical evidence for the functional similarity between human visual processing and the hierarchical feature evolution in deep neural networks.

Despite these advances, a limitation of our Shallow Alignment is that it still relies on a layer-wise sweep to identify the best intermediate representation. This suggests future directions, including developing adaptive layer selection mechanisms(e.g., via learnable gating) and exploring self-calibrating granularity alignment strategies.

References

- [1] Guillaume Alain and Yoshua Bengio. Understanding intermediate layers using linear classifier probes. *arXiv preprint arXiv:1610.01644*, 2016.
- [2] Alessio Ansuini, Alessandro Laio, Jakob H Macke, and Davide Zoccolan. Intrinsic dimension of data representations in deep neural networks. *Advances in Neural Information Processing Systems*, 32, 2019.
- [3] Thomas Carlson, David A Tovar, Arjen Alink, and Nikolaus Kriegeskorte. Representational dynamics of object vision: the first 1000 ms. *Journal of vision*, 13(10):1–1, 2013.
- [4] Zhe Chen, Jiannan Wu, Wenhui Wang, Weijie Su, Guo Chen, Sen Xing, Muyan Zhong, Qinglong Zhang, Xizhou Zhu, Lewei Lu, et al. Internvl: Scaling up vision foundation models and aligning for generic visual-linguistic tasks. In *Proceedings of the IEEE/CVF Conference on Computer Vision and Pattern Recognition*, pages 24185–24198, 2024.

[5] Mehdi Cherti, Romain Beaumont, Ross Wightman, Mitchell Wortsman, Gabriel Ilharco, Cade Gordon, Christoph Schuhmann, Ludwig Schmidt, and Jenia Jitsev. Reproducible scaling laws for contrastive language-image learning. In *Proceedings of the IEEE/CVF Conference on Computer Vision and Pattern Recognition*, pages 2818–2829, 2023.

[6] Radoslaw Martin Cichy, Dimitrios Pantazis, and Aude Oliva. Resolving human object recognition in space and time. *Nature neuroscience*, 17(3):455–462, 2014.

[7] James J DiCarlo, Davide Zoccolan, and Nicole C Rust. How does the brain solve visual object recognition? *Neuron*, 73(3):415–434, 2012.

[8] Alexey Dosovitskiy, Lucas Beyer, Alexander Kolesnikov, Dirk Weissenborn, Xiaohua Zhai, Thomas Unterthiner, Mostafa Dehghani, Matthias Minderer, Georg Heigold, Sylvain Gelly, et al. An image is worth 16x16 words: Transformers for image recognition at scale. In *International Conference on Learning Representations*, 2021.

[9] Utku Evci, Vincent Dumoulin, Hugo Larochelle, and Michael C Mozer. Head2toe: Utilizing intermediate representations for better transfer learning. In *International Conference on Machine Learning*, pages 6009–6033. PMLR, 2022.

[10] Yuxin Fang, Quan Sun, Xinggang Wang, Tiejun Huang, Xinlong Wang, and Yue Cao. Eva-02: A visual representation for neon genesis. *arXiv preprint arXiv:2303.11331*, 2023.

[11] Anupam K Garg, Peichao Li, Mohammad S Rashid, and Edward M Callaway. Color and orientation are jointly coded and spatially organized in primate primary visual cortex. *Science*, 364(6447):1275–1279, 2019.

[12] Alessandro T Gifford, Kshitij Dwivedi, Gemma Roig, and Radoslaw M Cichy. A large and rich eeg dataset for modeling human visual object recognition. *NeuroImage*, 264:119754, 2022.

[13] Alexandre Gramfort, Martin Luessi, Eric Larson, Denis A Engemann, Daniel Strohmeier, Christian Brodbeck, Lauri Parkkonen, and Matti S Hämäläinen. Mne software for processing meg and eeg data. *neuroimage*, 86:446–460, 2014.

[14] Tijl Grootswagers, Amanda K Robinson, and Thomas A Carlson. The representational dynamics of visual objects in rapid serial visual processing streams. *NeuroImage*, 188:668–679, 2019.

[15] Tijl Grootswagers, Ivy Zhou, Amanda K Robinson, Martin N Hebart, and Thomas A Carlson. Human eeg recordings for 1,854 concepts presented in rapid serial visual presentation streams. *Scientific Data*, 9(1):3, 2022.

[16] Kaiming He, Xiangyu Zhang, Shaoqing Ren, and Jian Sun. Deep residual learning for image recognition. In *Proceedings of the IEEE conference on computer vision and pattern recognition*, pages 770–778, 2016.

[17] Martin N Hebart, Oliver Contier, Lina Teichmann, Adam H Rockter, Charles Y Zheng, Alexis Kidder, Anna Corriveau, Maryam Vaziri-Pashkam, and Chris I Baker. Things-data, a multimodal collection of large-scale datasets for investigating object representations in human brain and behavior. *Elife*, 12:e82580, 2023.

[18] David H Hubel and Torsten N Wiesel. Receptive fields and functional architecture of monkey striate cortex. *The Journal of physiology*, 195(1):215–243, 1968.

[19] Gabriel Ilharco, Mitchell Wortsman, Ross Wightman, Cade Gordon, Nicholas Carlini, Rohan Taori, Achal Dave, Vaishaal Shankar, Hongseok Namkoong, John Miller, Hannaneh Hajishirzi, Ali Farhadi, and Ludwig Schmidt. Openclip, July 2021. If you use this software, please cite it as below.

[20] Salman Khan, Muzammal Naseer, Munawar Hayat, Syed Waqas Zamir, Fahad Shahbaz Khan, and Mubarak Shah. Transformers in vision: A survey. *ACM computing surveys (CSUR)*, 54(10s):1–41, 2022.

[21] Alex Krizhevsky, Ilya Sutskever, and Geoffrey E Hinton. Imagenet classification with deep convolutional neural networks. *Advances in neural information processing systems*, 25, 2012.

[22] Yoonho Lee, Annie S Chen, Fahim Tajwar, Ananya Kumar, Huaxiu Yao, Percy Liang, and Chelsea Finn. Surgical fine-tuning improves adaptation to distribution shifts. *arXiv preprint arXiv:2210.11466*, 2022.

[23] Dongyang Li, Chen Wei, Shiying Li, Jiachen Zou, Haoyang Qin, and Quanying Liu. Visual decoding and reconstruction via eeg embeddings with guided diffusion. *arXiv preprint arXiv:2403.07721*, 2024.

[24] Yueyang Li, Zijian Kang, Shengyu Gong, Wenhao Dong, Weiming Zeng, Hongjie Yan, Wai Ting Siok, and Nizhuan Wang. Neural-mcrl: Neural multimodal contrastive representation learning for eeg-based visual decoding. *arXiv preprint arXiv:2412.17337*, 2024.

[25] Liang Liang, Alex Fratzl, Glenn Goldey, Rohan N Ramesh, Arthur U Sugden, Josh L Morgan, Chinfei Chen, and Mark L Andermann. A fine-scale functional logic to convergence from retina to thalamus. *Cell*, 173(6):1343–1355, 2018.

[26] Aravindh Mahendran and Andrea Vedaldi. Understanding deep image representations by inverting them. In *Proceedings of the IEEE conference on computer vision and pattern recognition*, pages 5188–5196, 2015.

[27] Leland McInnes, John Healy, and James Melville. Umap: Uniform manifold approximation and projection for dimension reduction. *arXiv preprint arXiv:1802.03426*, 2018.

[28] Ian Nauhaus, Kristina J Nielsen, Anita A Disney, and Edward M Callaway. Orthogonal micro-organization of orientation and spatial frequency in primate primary visual cortex. *Nature neuroscience*, 15(12):1683–1690, 2012.

[29] Maxime Oquab, Timothée Darcet, Théo Moutakanni, Huy Vo, Marc Szafraniec, Vasil Khalidov, Pierre Fernandez, Daniel Haziza, Francisco Massa, Alaaeldin El-Nouby, et al. Dinov2: Learning robust visual features without supervision. *Transactions on Machine Learning Research*, 2024.

[30] Vardan Petyan, XY Han, and David L Donoho. Prevalence of neural collapse during the terminal phase of deep learning training. *Proceedings of the National Academy of Sciences*, 117(40):24652–24663, 2020.

[31] Alec Radford, Jong Wook Kim, Chris Hallacy, Aditya Ramesh, Gabriel Goh, Sandhini Agarwal, Girish Sastry, Amanda Askell, Pamela Mishkin, Jack Clark, et al. Learning transferable visual models from natural language supervision. In *International conference on machine learning*, pages 8748–8763. PMLR, 2021.

- [32] Yonghao Song, Bingchuan Liu, Xiang Li, Nanlin Shi, Yijun Wang, and Xiaorong Gao. Decoding natural images from eeg for object recognition. *arXiv preprint arXiv:2308.13234*, 2023.
- [33] Yonghao Song, Yijun Wang, Huiguang He, and Xiaorong Gao. Recognizing natural images from eeg with language-guided contrastive learning. *IEEE Transactions on Neural Networks and Learning Systems*, 2025.
- [34] Concetto Spampinato, Simone Palazzo, Isaak Kavasidis, Daniela Giordano, Nasim Souly, and Mubarak Shah. Deep learning human mind for automated visual classification. In *Proceedings of the IEEE conference on computer vision and pattern recognition*, pages 6809–6817, 2017.
- [35] Jose Antonio Urigüen and Begoña García-Zapirain. Eeg artifact removal—state-of-the-art and guidelines. *Journal of neural engineering*, 12(3):031001, 2015.
- [36] Arnas Uselis and Seong Joon Oh. Intermediate layer classifiers for ood generalization. *arXiv preprint arXiv:2504.05461*, 2025.
- [37] David C Van Essen, Charles H Anderson, and Daniel J Felleman. Information processing in the primate visual system: an integrated systems perspective. *Science*, 255(5043):419–423, 1992.
- [38] Yisen Wang, Xingjun Ma, Zaiyi Chen, Yuan Luo, Jinfeng Yi, and James Bailey. Symmetric cross entropy for robust learning with noisy labels. In *Proceedings of the IEEE/CVF international conference on computer vision*, pages 322–330, 2019.
- [39] Haitao Wu, Qing Li, Changqing Zhang, Zhen He, and Xiaomin Ying. Bridging the vision-brain gap with an uncertainty-aware blur prior. In *Proceedings of the Computer Vision and Pattern Recognition Conference*, pages 2246–2257, 2025.
- [40] Daniel LK Yamins and James J DiCarlo. Using goal-driven deep learning models to understand sensory cortex. *Nature neuroscience*, 19(3):356–365, 2016.
- [41] Matthew D Zeiler and Rob Fergus. Visualizing and understanding convolutional networks. In *European conference on computer vision*, pages 818–833. Springer, 2014.
- [42] Xiaohua Zhai, Alexander Kolesnikov, Neil Houlsby, and Lucas Beyer. Scaling vision transformers. In *Proceedings of the IEEE/CVF Conference on Computer Vision and Pattern Recognition*, pages 12104–12113, 2022.
- [43] Kaifan Zhang, Lihuo He, Xin Jiang, Wen Lu, Di Wang, and Xinbo Gao. Cognitioncapturer: Decoding visual stimuli from human eeg signal with multimodal information. In *Proceedings of the AAAI Conference on Artificial Intelligence*, volume 39, pages 14486–14493, 2025.
- [44] Wenjiang Zhang, Sifeng Wang, Yuwei Su, Xinyu Li, Chen Zhang, and Suyu Zhong. Neurobridge: Bio-inspired self-supervised eeg-to-image decoding via cognitive priors and bidirectional semantic alignment. *arXiv preprint arXiv:2511.06836*, 2025.

A Experimental Details

A.1 Datasets for Experiments

THINGS-EEG. We conduct experiments on the THINGS-EEG dataset, which contains electroencephalography (EEG) recordings from 10 human subjects performing a visual recognition task under a Rapid Serial Visual Presentation (RSVP) paradigm. Each subject participates in four experimental sessions. The training set consists of 1,654 concepts, with each concept represented by 10 unique images, and each image repeated four times, resulting in 16,540 trials per subject. The test set includes 200 unseen concepts, each represented by a single image repeated 80 times, which are averaged to obtain one trial per concept, yielding 200 test samples per subject.

EEG signals are recorded at a sampling rate of 1000 Hz and band-pass filtered between 0.1–100 Hz. The continuous signals are segmented into epochs from 0 to 1000 ms relative to stimulus onset, with baseline correction performed using the mean signal within the 200 ms pre-stimulus interval. The epoched data are then downsampled to 250 Hz for subsequent processing. To improve signal-to-noise ratio (SNR), repetitions of the same stimulus are averaged in both the training and test sets. All preprocessed EEG data are stored in `float32` format to balance storage efficiency and computational performance. For all experiments, we restrict EEG channels to those over the occipital and parietal lobes, which are closely associated with visual perception and visuospatial processing.

THINGS-MEG. We further evaluate our method on the THINGS-MEG dataset, which contains magnetoencephalography (MEG) recordings from four human participants performing the same visual recognition task. The training set comprises 1,854 concepts, each associated with 12 distinct images, with one trial per image. The test set includes 200 concepts, each represented by a single image repeated 12 times, which are averaged to obtain one trial per concept. To ensure a zero-shot evaluation setting, all test concepts are entirely excluded from the training set.

MEG signals are recorded from 271 sensors at a sampling rate of 1000 Hz. Each trial includes a 500 ms stimulus presentation followed by an inter-stimulus interval of 1000 ± 200 ms. The continuous MEG recordings are segmented into epochs spanning 0 to 1000 ms after stimulus onset. A band-pass filter of 0.1–100 Hz is applied, followed by baseline correction using the mean signal from the 200 ms pre-stimulus window. The epoched signals are subsequently downsampled to 200 Hz. To enhance SNR, all repetitions corresponding to the same test image are averaged. Channel-wise z-score normalization is applied across trials. The final preprocessed MEG data are stored in `float32` format to reduce storage requirements and improve I/O efficiency during training and evaluation. For all experiments, we also restrict MEG channels to those over the occipital and parietal lobes.

A.2 EEG Encoder Architectures

We evaluate several distinct neural network architectures for EEG signal encoding, ranging from lightweight multi-layer perceptrons to hybrid Convolutional-Transformer models. The implementation details of each model are described below.

A.2.1 EEGProject

EEGProject serves as a lightweight baseline architecture, treating the EEG decoding task as a direct mapping problem without explicit temporal or spatial filtering layers.

- Input: The raw EEG signal $X \in \mathbb{R}^{B \times C \times T}$ is flattened into a vector of size $B \times (C \cdot T)$.

- Architecture: A Multi-Layer Perceptron (MLP) with a residual bottleneck. It consists of a linear layer, a GELU activation, dropout ($p = 0.3$), and a final LayerNorm.

A.2.2 EEGNet

EEGNet is a compact Convolutional Neural Network specifically designed for EEG signal processing, emphasizing depthwise and separable convolutions to extract temporal and spatial features efficiently.

- Temporal Block: A 2D convolution with kernel $(1, 64)$ captures high-frequency temporal information.
- Spatial Block: A depthwise convolution with kernel $(C, 1)$ learns spatial filters across EEG channels.
- Separable Block: After average pooling $(1, 2)$, a separable convolution with kernel $(1, 16)$ integrates features followed by ELU activation and Dropout.
- Projection: The output is flattened and passed through a residual MLP block with LayerNorm to produce the final embedding.

A.2.3 ATM (Adaptive Thinking Mapper)

The ATM model is a hybrid architecture that integrates an inverted Transformer backbone with a convolutional patch embedding module.

- Backbone (iTransformer): The backbone adopts an iTransformer-style architecture designed for multivariate time-series modeling. Given an input $X \in \mathbb{R}^{B \times C \times T}$, each time step is first mapped into a latent representation with frequency-aware positional encoding, and the resulting sequence is processed by a self-attention encoder with four attention heads and a single encoder block to capture long-range temporal dependencies across channels.
- Patch Embedding: The output of the transformer is passed to a convolutional block inspired by ShallowNet. It consists of:
 1. Temporal Convolution: Kernel $(1, 25)$, Stride $(1, 1)$.
 2. Average Pooling: Kernel $(1, 51)$, Stride $(1, 5)$.
 3. Spatial Convolution: Kernel $(C, 1)$, mapping channel interactions.
- Projection: A residual projection head maps the flattened features to the target latent dimension.

A.2.4 EEGConformer

EEGConformer combines the local feature extraction capabilities of Convolutional Neural Networks with the global context modeling of Transformers.

- Patch Embedding: Utilizes a ShallowNet-like structure (similar to ATMS) with temporal convolution $(1, 25)$ and pooling $(1, 51)$ to downsample the signal and extract local features.
- Transformer Encoder: A stack of standard Transformer encoder blocks (default depth=2) processes the sequence of patches. Each block includes Multi-Head Self-Attention and a Feed-Forward Network with residual connections and LayerNorm.

- Projection Head: A linear projection head with BatchNorm and ELU activation maps the features to the contrastive learning space.

A.2.5 TSConv (Time-Space Convolution)

The TSConv encoder focuses purely on convolutional feature extraction without attention mechanisms.

- Architecture: It employs the same convolutional front-end as the PatchEmbedding module:
 1. Conv2d (1, 40) with kernel (1, 25) for temporal features.
 2. AvgPool2d (1, 51) with stride (1, 5) for downsampling.
 3. Conv2d (40, 40) with kernel (C , 1) for spatial aggregation.
- Output: The features are projected via a residual linear block to the target dimension.

A.2.6 Summary of Architecture Specifications

Table 3: Comparison of EEG Encoder Architectures and Key Hyperparameters.

Model	Core Mechanism	Temporal Kernel	Spatial Kernel	Attention Heads
ATM	iTransformer + CNN	(1, 25)	(C , 1)	4
EEGNet	Depthwise + Separable CNN	(1, 64)	(C , 1)	N/A
EEGConformer	CNN + Transformer	(1, 25)	(C , 1)	10
EEGProject	MLP (Flattened)	N/A	N/A	N/A
TSConv	Pure CNN	(1, 25)	(C , 1)	N/A

B Results Details

B.1 Top-1 retrieval accuracy of different vision backbones

Table 4 presents the top 1 performance of different vision backbones. Table 5 reports the intra-subject and inter-subject 200-way zero-shot retrieval accuracy on THINGS-EEG using the best-performing intermediate-layer features from different vision encoders. Overall, models with larger capacity and stronger pretraining consistently yield better decoding performance. Table 6 summarizes the decoding performance when using the final output representations of different vision encoders. Taken together, these results demonstrate that selecting appropriate intermediate representations is crucial for visual neural decoding.

Table 4: Summary of intermediate-layer alignment performance across different backbones. We report the relative depth of the best-performing intermediate layer and the final output representation. The best layer is selected based on the highest Top-1 accuracy among all probed layers. For ResNet models, the final feature is obtained by attention pooling of the last convolutional layer. For Transformer-based models, the final feature corresponds to the CLS token embedding from the last layer. Relative depth is computed as $(\ell - 1)/(L - 1)$. Δ denotes the Top-1 accuracy gain of the best intermediate layer over the final output representation.

Model	Params	#Layers	Best ℓ	Best Depth (%)	Acc of Best Layer (%)	Acc of Final Output (%)	Δ (%)
RN50	38M	4	3	66.7	67.7	40.3	+27.4
RN101	56M	4	3	66.7	59.2	36.5	+22.7
ViT-B-16	86M	12	6	45.5	68.6	37.1	+31.5
ViT-H-14	632M	32	11	32.3	76.8	33.5	+43.3
DINOv2	1.14B	40	16	38.5	75.9	17.5	+58.4
ViT-bigG-14	1.84B	48	27	55.3	75.2	33.2	+42.0
EVA-02	4.35B	64	35	54.0	79.0	37.9	+41.1
InternViT	5.54B	46	28	60.0	82.6	55.9	+26.7

Table 5: Accuracy (%) of 200-way zero-shot retrieval on THINGS-EEG using the best intermediate-layer representations from different vision encoders.

Method	Metric	Sub1	Sub2	Sub3	Sub4	Sub5	Sub6	Sub7	Sub8	Sub9	Sub10	Avg.
Intra-Subject: train and test on one subject												
RN50	Top-1	62.9	63.3	68.1	67.7	58.9	70.6	65.6	72.1	66.1	81.9	67.7
	Top-5	89.5	92.2	91.8	91.4	87.0	93.1	91.1	94.3	90.8	97.1	91.8
RN101	Top-1	48.4	56.5	58.9	60.5	48.2	62.9	61.7	66.4	59.0	69.8	59.2
	Top-5	81.3	87.3	87.1	88.3	80.1	88.4	85.3	89.1	84.9	94.2	86.6
ViT-B-16	Top-1	63.6	68.3	69.0	67.3	61.1	73.0	68.6	70.4	66.3	78.3	68.6
	Top-5	91.8	93.9	92.2	93.1	88.4	94.9	94.6	95.2	90.9	96.9	93.2
ViT-H-14	Top-1	69.4	78.9	78.6	73.1	68.7	81.1	78.4	80.1	75.0	85.0	76.8
	Top-5	92.2	97.1	96.4	96.4	94.2	97.5	96.1	98.4	94.7	97.4	96.0
DINOv2	Top-1	67.7	77.9	76.0	72.7	69.7	81.9	74.1	79.1	75.6	84.7	75.9
	Top-5	92.2	95.5	96.2	95.0	92.2	98.2	96.2	98.5	95.2	98.3	95.8
ViT-bigG-14	Top-1	65.3	75.1	74.4	75.3	67.7	82.7	74.3	79.8	70.9	86.8	75.2
	Top-5	90.8	95.0	95.5	96.4	92.7	97.0	94.8	98.3	92.8	95.9	94.9
EVA-02	Top-1	70.8	81.9	80.7	77.6	74.3	84.2	76.8	82.7	75.8	85.2	79.0
	Top-5	92.8	97.7	95.9	98.2	94.5	97.4	95.6	98.6	96.0	98.5	96.5
InternViT	Top-1	75.0	87.5	83.2	79.5	74.6	89.9	78.5	86.9	81.3	89.3	82.6
	Top-5	94.3	98.9	98.2	96.1	96.4	99.3	97.3	99.4	97.8	99.1	97.7
Inter-Subject: leave one subject out for test												
RN50	Top-1	16.7	24.4	7.6	18.1	13.4	14.0	14.5	15.7	17.7	22.2	16.4
	Top-5	42.0	51.1	27.3	43.4	41.4	37.5	36.7	38.8	44.4	52.1	41.5
RN101	Top-1	16.2	22.0	8.3	15.9	13.0	13.4	11.1	13.3	16.7	21.8	15.2
	Top-5	38.3	49.2	28.1	42.0	37.4	38.1	33.3	36.7	43.3	51.8	39.8
ViT-B-16	Top-1	18.3	23.7	7.4	17.8	14.1	12.1	14.4	15.0	17.6	22.7	16.3
	Top-5	42.8	52.1	26.3	45.1	40.0	39.3	38.4	36.1	46.1	54.7	42.1
ViT-H-14	Top-1	21.6	28.5	10.3	20.2	16.5	16.0	16.9	16.1	18.9	24.5	19.0
	Top-5	48.4	59.6	26.3	45.4	43.6	40.4	40.5	36.6	46.6	55.1	44.2
DINOv2	Top-1	23.2	26.7	11.2	18.8	18.0	16.6	16.8	13.2	18.9	23.3	18.7
	Top-5	53.4	60.6	29.0	45.4	44.8	43.5	45.4	36.8	49.1	56.0	46.4
ViT-bigG-14	Top-1	19.0	30.0	16.0	19.0	17.0	20.0	16.5	14.0	22.5	33.5	20.8
	Top-5	56.5	57.5	31.0	44.0	41.5	48.5	38.0	40.0	56.0	57.5	47.0
EVA-02	Top-1	20.8	26.5	11.5	18.8	18.9	18.8	14.5	17.8	20.5	24.8	19.3
	Top-5	50.9	57.2	29.0	45.2	44.7	46.6	41.2	40.2	53.6	53.8	46.2
InternViT	Top-1	23.5	30.6	10.0	19.5	18.1	22.7	18.6	17.3	23.0	34.4	21.8
	Top-5	53.2	60.4	28.1	48.3	45.2	49.8	46.0	46.1	54.8	62.0	49.4

Table 6: Accuracy (%) of 200-way zero-shot retrieval on THINGS-EEG using the final representations from different vision encoders.

Method	Metric	Sub1	Sub2	Sub3	Sub4	Sub5	Sub6	Sub7	Sub8	Sub9	Sub10	Avg.
Intra-Subject: train and test on one subject												
RN50	Top-1	26.3	38.9	42.1	40.7	32.2	46.8	39.0	47.9	36.0	53.0	40.3
	Top-5	59.9	72.1	78.5	75.5	65.5	77.5	70.1	79.9	70.6	85.7	73.5
RN101	Top-1	28.9	35.3	35.9	34.8	30.2	38.8	35.8	43.1	33.9	48.5	36.5
	Top-5	59.8	66.6	71.8	72.0	60.6	72.2	69.9	75.7	69.4	82.2	70.0
ViT-B-16	Top-1	28.5	35.0	39.8	36.2	29.0	40.8	36.2	41.1	35.2	49.1	37.1
	Top-5	58.8	68.7	72.8	71.9	59.1	72.5	70.3	76.2	66.9	83.2	70.1
ViT-H-14	Top-1	23.6	29.0	38.9	35.9	26.0	36.1	29.2	40.6	31.9	44.2	33.5
	Top-5	52.7	63.8	67.1	65.0	55.7	69.1	63.7	71.8	64.2	76.4	65.0
DINOv2	Top-1	11.9	16.0	18.6	18.4	12.0	17.3	17.4	23.0	17.2	23.2	17.5
	Top-5	30.2	40.1	46.5	42.5	32.1	41.3	40.7	47.8	39.6	47.7	40.9
ViT-bigG-14	Top-1	20.7	31.1	36.8	30.3	27.9	38.4	32.9	40.0	30.0	43.8	33.2
	Top-5	49.4	65.5	70.2	64.2	51.9	75.4	63.5	71.6	66.8	78.1	65.7
EVA-02	Top-1	28.7	36.6	41.1	36.6	28.6	40.8	38.6	42.6	36.0	49.8	37.9
	Top-5	55.9	67.7	73.1	71.0	60.8	76.2	69.5	76.0	64.6	81.9	69.7
InternViT	Top-1	44.1	54.4	56.3	57.4	46.4	59.0	52.5	64.3	53.8	71.2	55.9
	Top-5	76.5	82.5	88.5	87.0	76.9	90.4	85.0	90.6	84.3	94.9	85.7
Inter-Subject: leave one subject out for test												
RN50	Top-1	9.6	12.7	4.6	11.7	7.7	7.7	9.2	9.6	8.7	11.3	9.3
	Top-5	29.8	35.2	19.8	30.5	24.6	26.7	26.6	27.1	29.6	33.6	28.4
RN101	Top-1	9.3	12.9	3.3	11.1	6.7	6.1	7.3	8.0	4.2	12.7	8.1
	Top-5	25.4	35.1	17.1	30.8	20.0	23.9	24.0	22.4	20.9	35.0	25.5
ViT-B-16	Top-1	9.5	12.6	3.6	11.4	6.8	7.8	8.3	6.9	6.2	14.4	8.7
	Top-5	26.4	32.5	15.6	28.4	23.0	24.1	24.6	26.0	23.8	37.8	26.2
ViT-H-14	Top-1	8.0	10.2	5.2	12.0	5.4	6.2	4.7	7.4	7.3	11.3	7.8
	Top-5	23.9	26.2	15.6	31.2	17.2	22.1	23.0	20.9	20.8	34.2	23.5
DINOv2	Top-1	5.7	8.8	5.3	7.0	4.2	6.0	5.0	6.1	5.7	7.3	6.1
	Top-5	20.1	24.5	13.9	20.9	16.2	18.4	16.1	18.5	17.7	25.4	19.2
ViT-bigG-14	Top-1	8.0	10.3	5.3	7.8	5.5	10.0	7.0	7.0	7.0	8.5	7.6
	Top-5	24.8	29.0	18.8	28.5	22.0	25.5	25.0	24.5	23.0	32.3	25.3
EVA-02	Top-1	9.9	11.6	4.5	10.6	5.7	8.1	6.2	7.6	8.2	12.1	8.5
	Top-5	26.9	30.7	17.8	32.7	24.2	25.6	24.7	28.6	26.9	34.9	27.3
InternViT	Top-1	16.0	19.7	8.0	14.2	10.0	10.4	10.4	12.6	15.2	19.6	13.6
	Top-5	40.2	45.7	25.0	40.3	31.5	37.2	30.3	33.3	42.2	45.7	37.2

B.2 Analysis of Layer-wise Training Dynamics

To validate the impact of feature granularity, we analyze the training and testing loss curves across different layers of the InternViT encoder, as shown in Figure 8. The optimization landscapes reveal three distinct behaviors:

- Shallow Layers (e.g., Layers 4–12): These layers converge slowly and plateau at a higher testing loss, indicating that low-level features alone lack sufficient semantic discriminability for effective retrieval.
- Optimal Intermediate Layers (e.g., Layers 24–28): The most favorable dynamics emerge in the middle layers. Specifically, Layer 28 achieves the lowest testing loss among all candidates and maintains a minimal gap between training and testing curves. This tight generalization bound confirms that intermediate representations possess the superior granularity—balancing semantic abstraction with necessary texture details—to align with neural signals.
- Deep Layers (e.g., Layer 40–Final): Deeper layers exhibit signs of severe overfitting. While the training loss drops rapidly to near-zero, the test loss (orange) remains significantly high. This large generalization gap supports our "Granularity Mismatch" hypothesis: the highly compressed, invariant features at the end of large models are too abstract for the noisy neural signals to predict effectively.

In conclusion, the loss analysis corroborates our quantitative results: simply scaling up model depth does not guarantee better decoding. Instead, selecting the granularity-matched intermediate layer is crucial for preventing overfitting and achieving robust alignment.

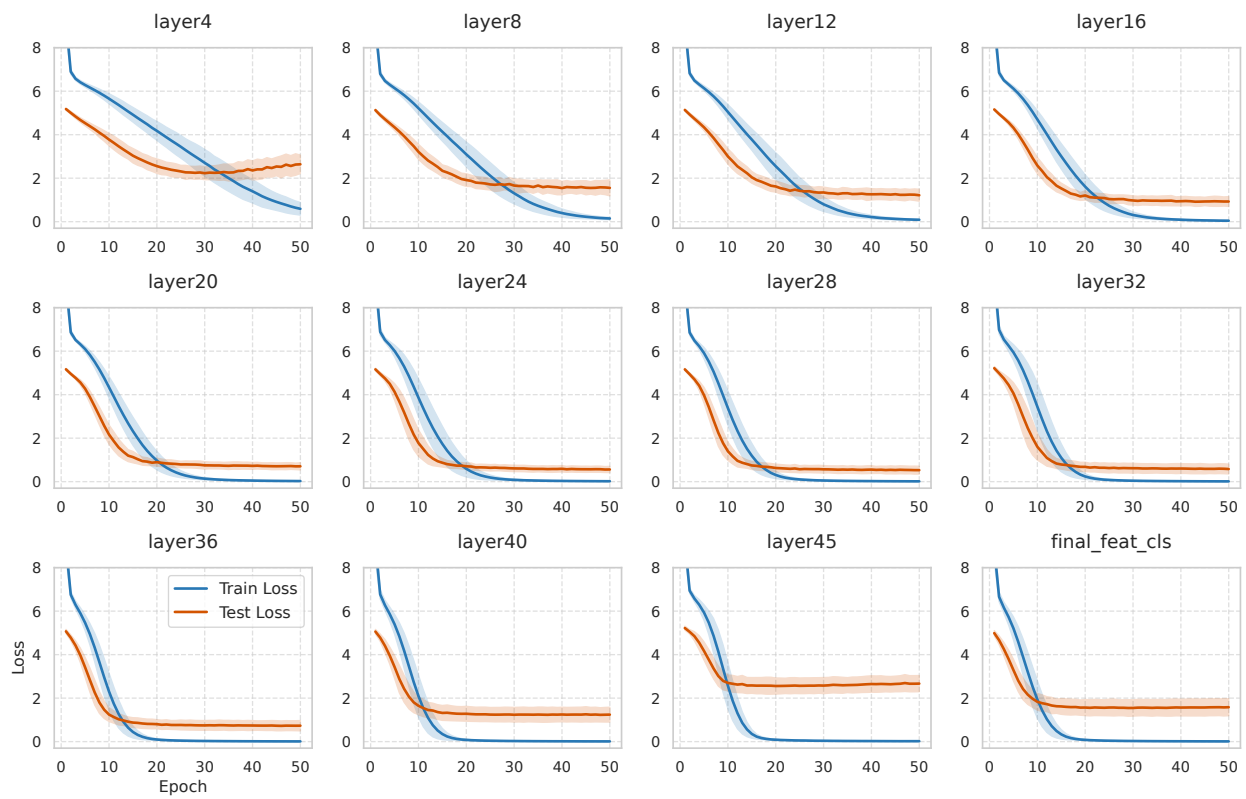


Figure 8: Layer-wise training dynamics on InternViT.

B.3 Umap Analysis

As shown in Figure 9, we can see that the two modalities gradually transition from being well separated at early layers to achieving the strongest mixing and alignment at intermediate layers (e.g., Layers 20–32), indicating that representations at these depths are most consistent with the intrinsic structure of neural signals. However, as the network deepens toward the final output layer, the feature distributions become separated again, further suggesting a granularity mismatch between the model’s highly abstract semantic representations and the human visual representations that retain rich fine-grained details.

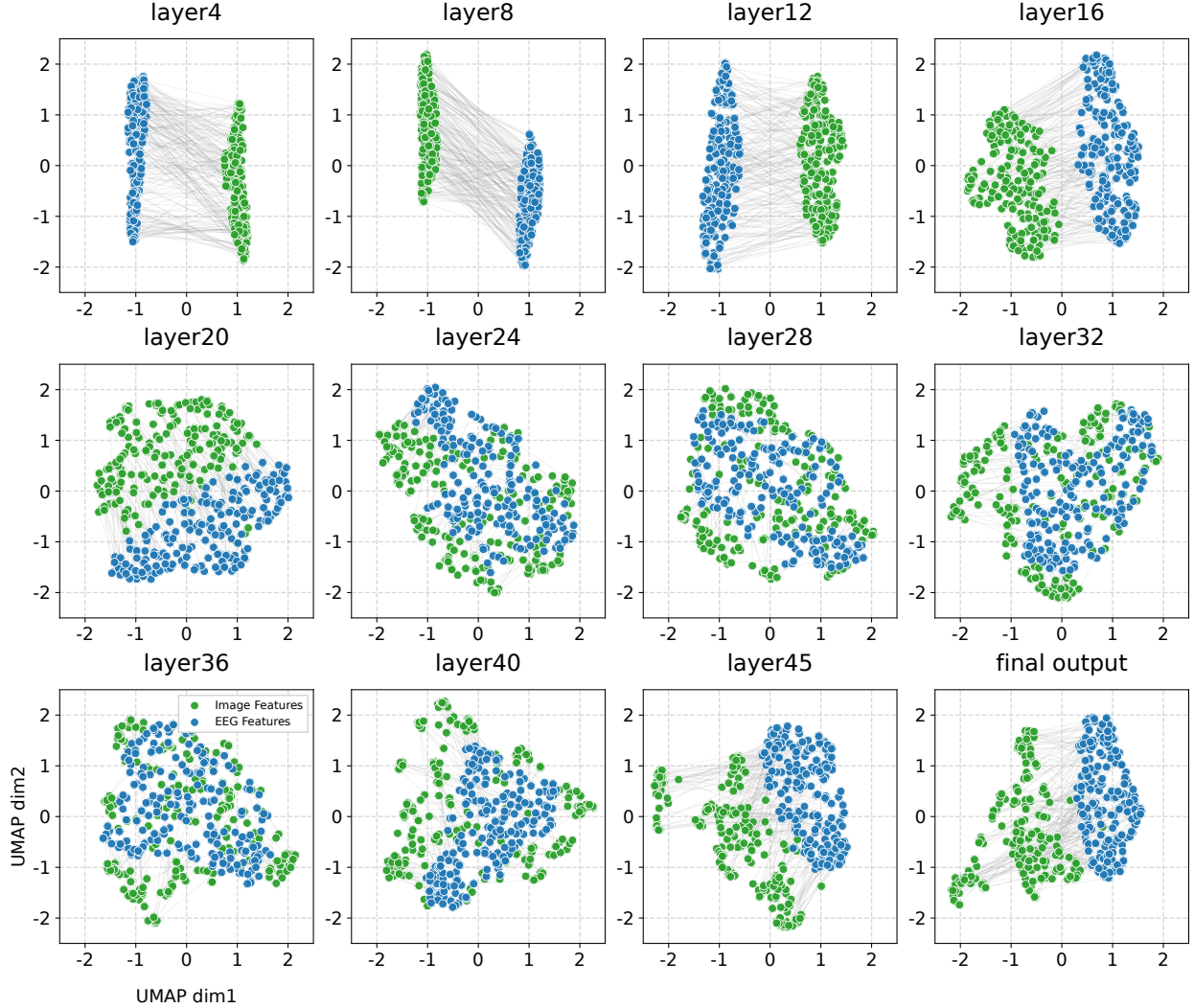


Figure 9: UMAP visualization of cross-modal alignment on THINGS-EEG (Subject 7). Illustration of alignment between image and EEG features on the test set of Subject 7 from the THINGS-EEG dataset, consisting of 200 samples. Image features are extracted from InternViT, while EEG features are obtained from the neural encoder. Each gray line connects a paired image–EEG sample.

B.4 Retrieval Case

We present more top-5 retrieval results on THINGS-EEG dataset in Figure 10, 11, 12, and 13, respectively. Our results indicate that fine-grained differences exist not only between different layers of the vision encoder, but also across subjects.

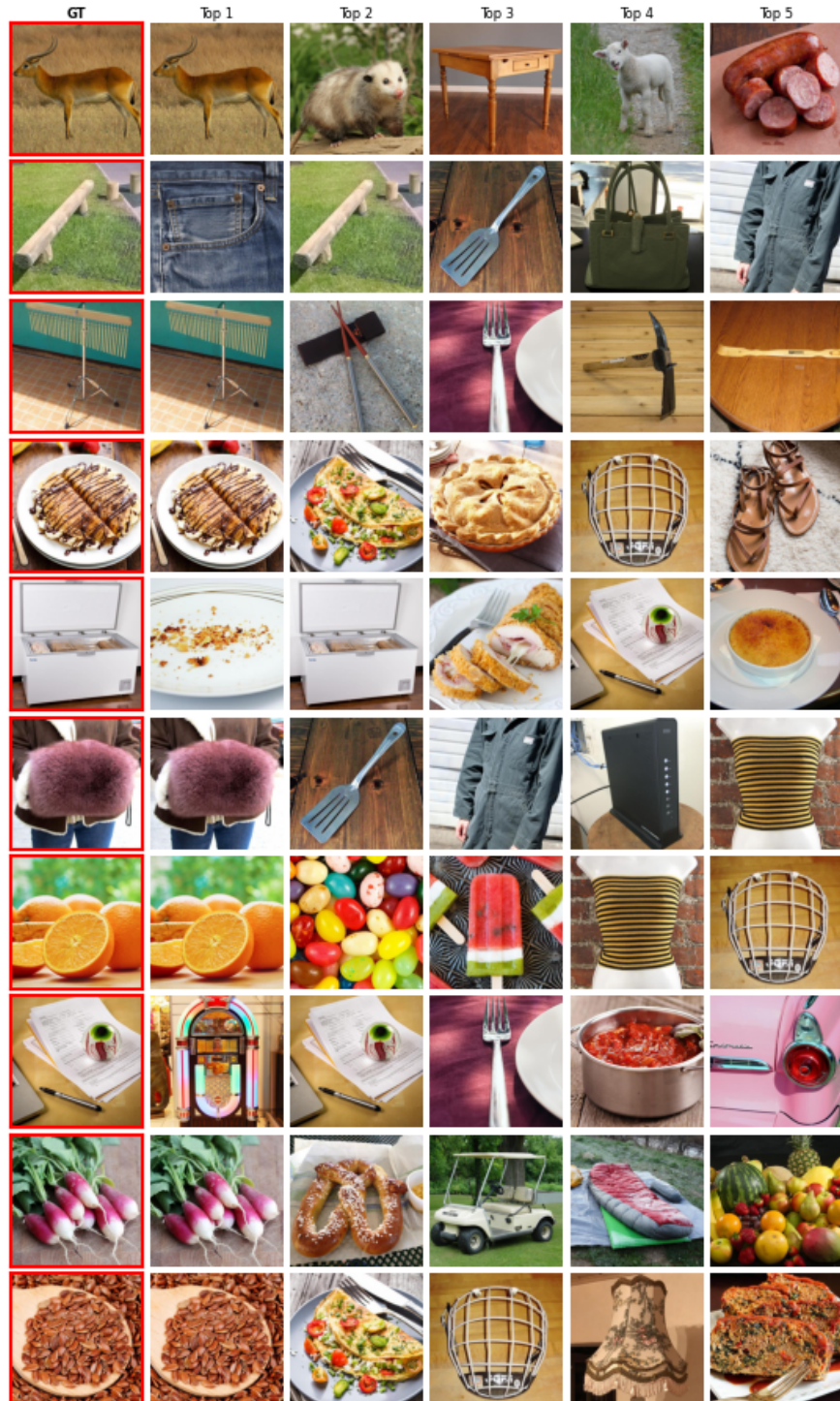


Figure 10: More top-5 retrieved samples of Subject 7 based on the best intermediate-layer embeddings.

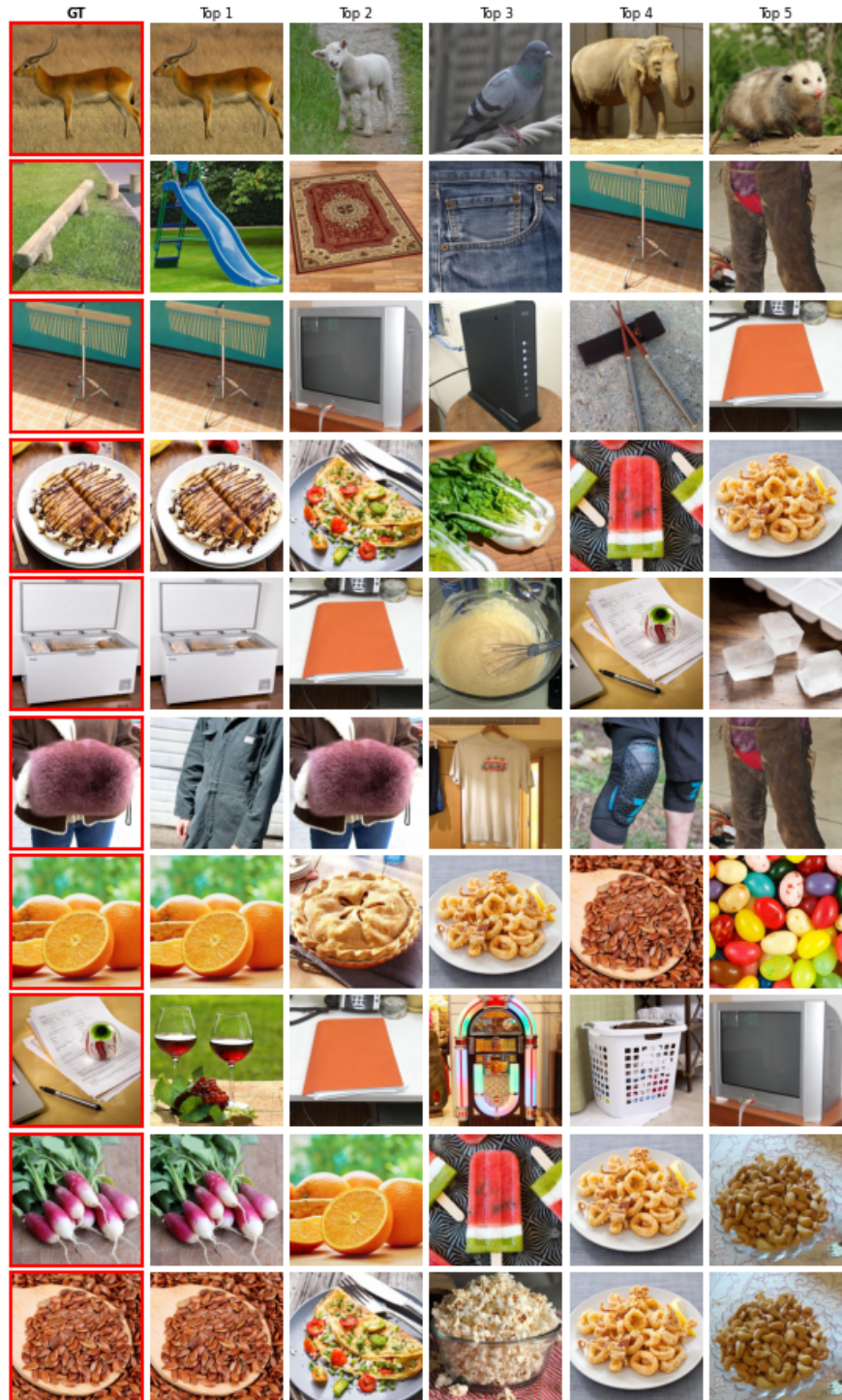


Figure 11: More top-5 retrieved samples of Subject 7 based on the final output embedding.

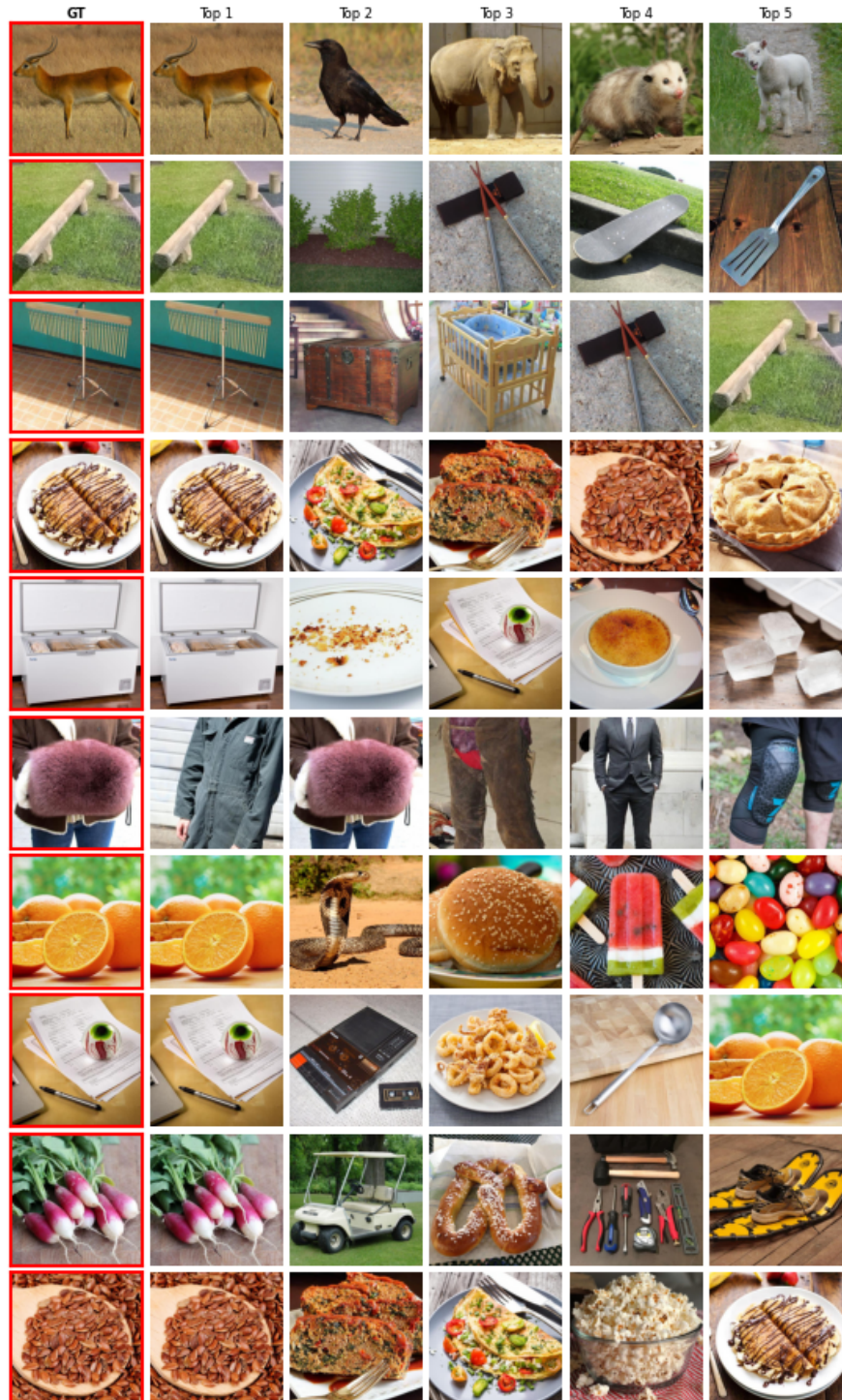


Figure 12: More top-5 retrieved samples of Subject 10 based on the best intermediate-layer embeddings.

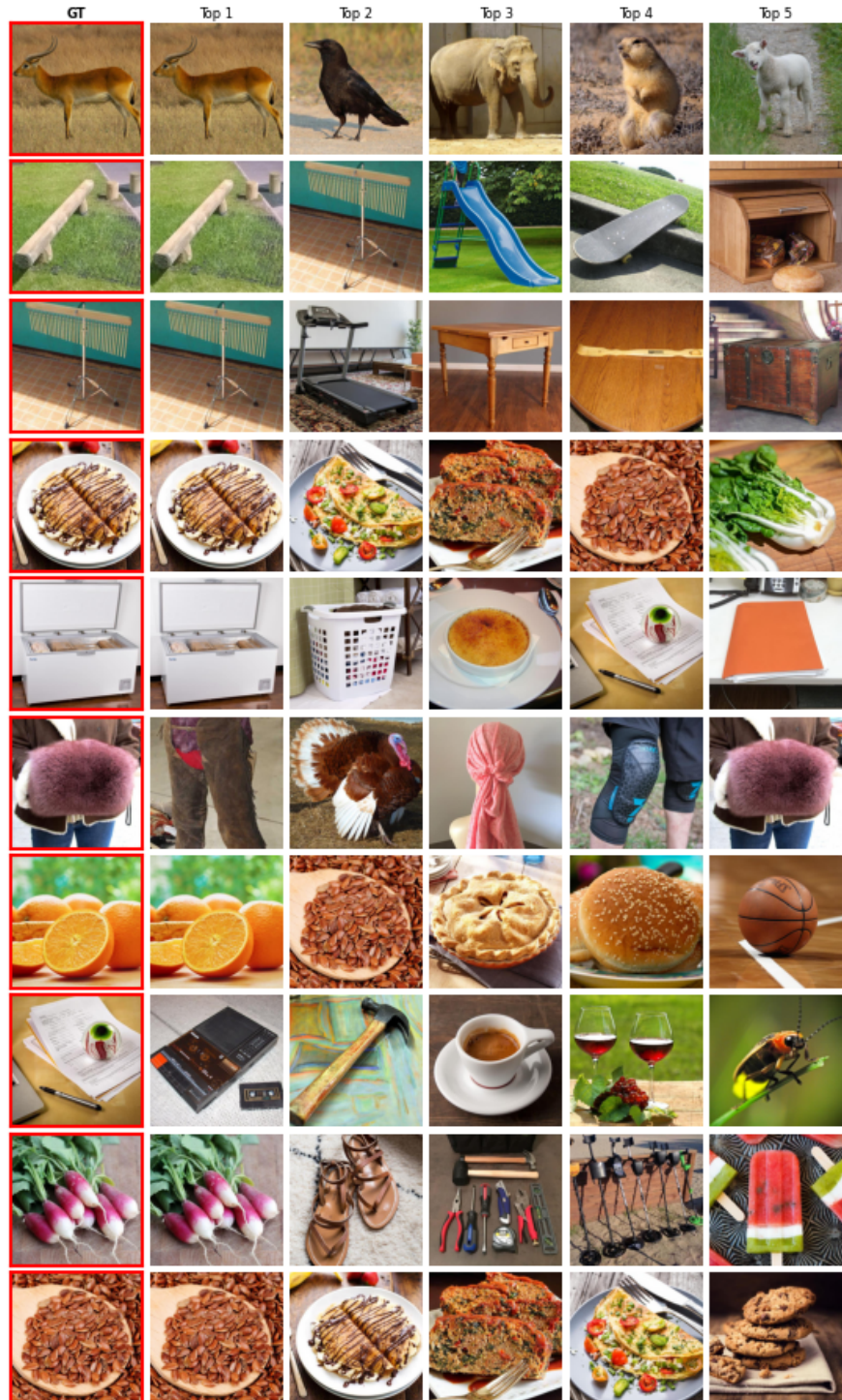


Figure 13: More top-5 retrieved samples of Subject 10 based on the final output embedding.